Integrating Dual-Channel Data Into the *d-q* Frame for Talkative Power Converters in Three-Phase AC Systems

Keming Liu, *Graduate Student Member, IEEE*, Yue Zhu, *Member, IEEE*, Yunjie Gu, *Senior Member, IEEE*, Jiande Wu, *Senior Member, IEEE*, Ruichi Wang, *Senior Member, IEEE*, and Xiangning He, *Fellow, IEEE*

***Abstract*—Talkative power converters (TPCs), capable of simultaneous power conversion and data modulation, have emerged as a hardware-minimized communication solution for power electronic systems. Although TPCs have been extensively studied in dc systems, their implementation in three-phase ac systems remains underexplored. This article proposes a novel dual-channel decoupled data modulation, which enables three-phase dc/ac TPCs to realize data interaction using two independent communication channels through power cables. The cross-axis coupling issue between the data transmitter and receiver is analyzed using a TPC communication model. To solve the problem, an adaptive estimation strategy is proposed to estimate and eliminate the coupling for each data frame. The proposed solution can be seamlessly deployed as a software upgrade compatible with existing three-phase inverters. Finally, experimental validation is conducted on a 3.3 kW ac microgrid comprising three grid-forming inverters, demonstrating the effectiveness and practical feasibility of the proposed approach.**

***Index Terms*—Cross-axis coupling interference, dual-channel data modulation, talkative power conversion, three-phase ac system.**

I. Introduction

THE increasing penetration of inverter-based resources (IBRs) in power systems poses significant challenges to system condition monitoring, IBR cooperative control, and real-time stability assessment [1], [2], [3], [4]. The solution to these challenges relies on reliable communication links among different IBRs and between IBRs and the substations.

Different communication technologies, including wired, wireless, and power line communication (PLC), have been applied to establish the communication link. However, both wired and wireless communication technologies have certain defects and would require additional installation and maintenance costs. Although PLC offers a cost-effective alternative by utilizing existing power lines for data transmission, its need for additional coupling circuits and signal processing hardware presents challenges in implementation and installation [5].

In recent years, an emerging technology known as power and signal dual modulation has gained increasing attention for its capacity to convert power and modulate signals simultaneously [6], [7], [8]. The converter that performs this dual function is termed a talkative power converter (TPC). By modulating the driving signal of the converter, data can be embedded into the ripples of output voltage (optionally also the input voltage) and transmitted along the power line. TPC utilizes the existing converter for data modulation, which avoids the influence of dedicated communication infrastructure faults and improves reliability. In addition, it requires minimal additional hardware [9], reducing the system's cost and complexity. Furthermore, it can establish communication links with simple software upgrades, improving the system's scalability. Therefore, TPC is a promising solution for local data interaction in IBR-dominated power systems.

There are essentially two subcategories of TPC called TPC with switching carrier (TPC-SC) and TPC with controlled ripple (TPC-CR), depending on how the data is embedded, as shown in Fig. 1. In TPC-SC, the PWM carrier is modulated and reshaped to carry data while the power reference manages only power control. Using switching voltage/current ripples and their sideband harmonics as data carriers facilitates a relatively high communication rate. However, the signal strength is inherently limited and lacks adjustability, thereby restricting its application range. In TPC-CR, the modulated data carrier is superimposed onto the power reference and subsequently compared to the pulsewidth modulation (PWM) carrier, enabling flexible adjustment of signal strength. The maximum data carrier frequency must not exceed half of the switching frequency.

TPC has been extensively investigated in various scenarios such as photovoltaic systems [10], [11], battery

Received 11 March 2025; revised 26 May 2025 and 22 July 2025; accepted 21 August 2025. Date of publication 27 August 2025; date of current version 13 November 2025. This work was supported in part by the National Natural Science Foundation of China under Grant 52350003, in part by the City University of Hong Kong under Grant 9382007, and in part by the NTU-Imperial Seed Fund. Recommended for publication by Associate Editor M. Chen. *(Corresponding author: Jiande Wu.)*

Keming Liu, Jiande Wu, and Xiangning He are with the College of Electrical Engineering, Zhejiang University, Hangzhou 310027, China (e-mail: liukeming@zju.edu.cn; eewjd@zju.edu.cn; hxn@zju.edu.cn).

Yue Zhu is with the Department of Electrical Engineering, City University of Hong Kong, SAR 999077, China (e-mail: yue.zhu@cityu.edu.hk).

Yunjie Gu is with the Department of Electrical and Electronic Engineering, Imperial College London, SW7 2AZ London, U.K. (e-mail: yunjie.gu@imperial.ac.uk).

Ruichi Wang is with the Wolfson School of Mechanical, Electrical and Manufacturing Engineering, Loughborough University, LE11 3TT Loughborough, U.K. (e-mail: rui_chi@163.com).

Color versions of one or more figures in this article are available at https://doi.org/10.1109/TPEL.2025.3603196.

Digital Object Identifier 10.1109/TPEL.2025.3603196

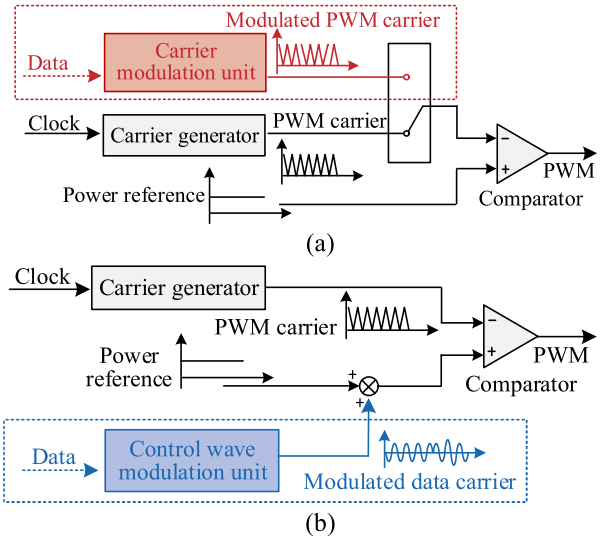

Fig. 1. (a) PWM modulation diagram of TPC-SC. (b) PWM modulation diagram of TPC-CR.

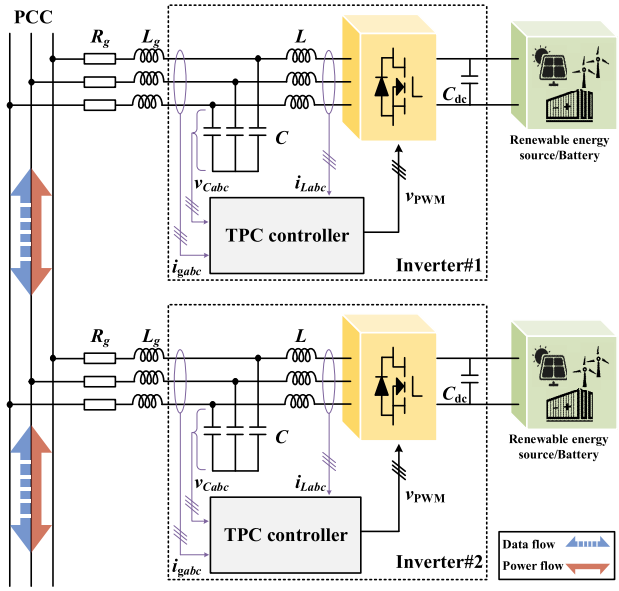

Fig. 2. Structure of the simplified two-node TPC system.

management systems [12], low-voltage power grids [13], and dc microgrids [14]. Innovated modulation strategies, e.g., orthogonal frequency division multiplexing [15], [16], multidegree-of-freedom modulation [17], [18], [19], and coded modulation [20] are also extended to TPC to increase communication rate. However, among these TPC applications, the emphasis is placed on dc systems, and limited work has investigated TPC in ac systems.

Given the advantages of TPC and the prevalence of three-phase ac power systems, it is appealing to use three-phase TPC. Recently, attempts have been made to implement TPC, including TPC-SC [21], [22], [23] and TPC-CR [24], [25] in three-phase ac systems. In [21], a variable zero-vector-width space vector PWM scheme is employed for data modulation, achieving a communication rate of 50 bits per second (bps), which is extremely low compared with TPC in dc systems. In [22], a communication rate of 600 bps is realized between a three-phase inverter and a motor. However, this method requires additional switching devices for signal modulation and hence increases the cost. In [23], a sideband harmonic-based TPC scheme is introduced to facilitate power quality-friendly signal transmission. For ac power systems where converters are far from each other and the line impedance is high, the high-frequency switching ripple from the converters can be significantly attenuated and becomes challenging for others to identify; hence, TPC-SC is inapplicable, and TPC-CR is preferred in such cases. In [24], data modulation is achieved by injecting fractional harmonic data carriers into the primary control loop using ON/OFF keying (OOK). The experimentally verified communication rate is only 5 bps with a low switching frequency utilization. In [25], 2FSK is employed to realize TPC, achieving a higher communication rate of 100 bps.

Accordingly, the TPC-CR methods mentioned above have low communication rate performances. In addition, the cross-axis coupling interference is presented between d–q frames at the data transmitter and receiver, which could result in TPC schemes failing and remaining unsolved. Furthermore, the multichannel TPC has not been researched, as only one communication channel has been used. To overcome the issues and fully exploit the potential of TPC in three-phase ac systems, a novel dual-channel decoupled data modulation scheme is proposed in this article. The main contributions of this article are as follows:

1) A dual-channel decoupled data modulation for TPC in three-phase ac systems is proposed, achieving dual-channel independent communication.
2) The TPC communication model is established, and an adaptive estimation strategy is proposed to estimate and eliminate the cross-axis coupling interference for each data frame.
3) A three-node three-phase TPC system has been established to validate the feasibility of the proposed scheme.

The rest of this article is organized as follows. Section II elucidates the fundamental concept of the proposed scheme. In Section III, the data transmission process and decoupling strategies are provided in detail. Section IV presents three-node experiments to validate both the theoretical framework and the practical feasibility of the proposed TPC scheme. Finally, Section V concludes this article.

II. Basic Concept of Proposed TPC Scheme

For a three-phase ac system, the proposed TPC scheme can help build the data link between any two inverters for status monitoring or control without extra communication hardware. Fig. 2 shows the simplified two-node TPC system structure, where two inverters are connected to the same point of common coupling. The inverters serve as the interface for both power and data, facilitating the transmission of power flow and data flow along the power line. The TPC controller of each inverter is tasked with either power control for a grid-following inverter or voltage control for a grid-forming inverter, together with

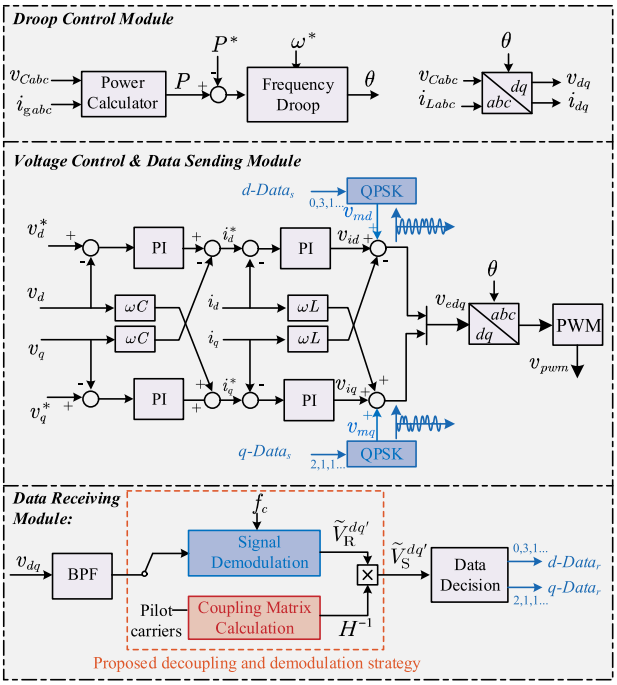

Fig. 3. TPC controller for an inverter equipped with frequency-droop controller.

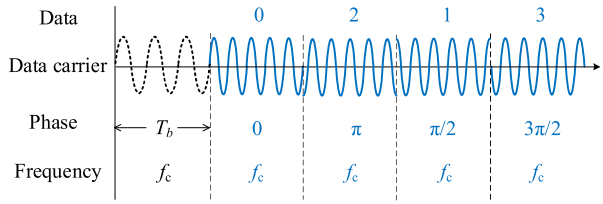

Fig. 4. Data modulation process.

the data exchange function. This article only discusses TPC implementation in grid-forming inverters, which are widely used for ac microgrids, while the same function can be easily extended to grid-following inverters.

The proposed TPC controller equipped with frequency-droop control is demonstrated in Fig. 3. It contains three modules: the droop controller, the voltage controller and data transmitter, and the data receiver. The droop controller module employs a power-frequency droop configuration, which sets the grid frequency (50 Hz in this article) and, in the meantime, provides the rotating angle θ for d–q frame transformation.

In the voltage control and data-transmitter module, the inductor current i_{dq} and the capacitor voltage v_{dq} are used for primary voltage control. When the inverter is required to transmit data, the data is first allocated to two independent data streams: d-$Data_s$ and q-$Data_s$, which are in quaternary format: 0, 1, 2, 3. Subsequently, these two data streams are modulated into sinusoidal waveforms, known as carrier signals, with a frequency of f_c using quadrature phase shift keying (QPSK), as shown in Fig. 4. When nonlinear loads or variable line impedances are present, the carrier frequency can be selectively chosen to avoid overlap with dominant harmonic components. The resulting carrier signals, denoted as v_{md} and v_{mq}, are superimposed onto the d–q frame voltage references v_{id} and v_{iq} to realize data carrier injection. It should be noted that using the d–q frame for data modulation can realize natural power balance by setting $v_0 = 0$ according to the dq-abc transformation. In addition, the power modulation signals in the d–q axes typically consist only of direct components, simplifying communication signal extraction and filter design. Followed by the dq-abc transformation and PWM modulation, the data can be integrated into the output voltage of the inverter and thereby received by other inverters.

To avoid the influence of injected carrier signals on voltage control, two principles must be followed. First, the ratio of the amplitudes of v_{md} and v_{id}, known as the modulation depth, should be minimized to reduce interference with the primary voltage control. Second, the data carrier frequency f_c must be chosen above the cut-off frequency of the control loop. From the communication perspective, increasing the data carrier frequency facilitates a higher communication rate. However, several practical limitations, such as the Nyquist limit and switching frequency constraints, the control resolution requirements, the effect of output filter characteristics, and the sampling rate of the receiver, must be carefully balanced when selecting an appropriate value for data carrier frequency f_c.

The data-receiving module is tasked with the extraction and restoration of data sent by other inverters. The module encompasses high-pass filtering (HPF), a specifically designed decoupling strategy that includes data demodulation, and the data decision process that identifies the quaternary data. The received signals are originally integrated into the capacitor voltage v_{Cabc} and transferred to v_{dq} via θ. However, θ created by each inverter is from its local reference frame and can be influenced by the power flow as well as the design of the droop controller. As a result, θ from different inverters will be largely different. The same situation also applies to grid-following inverters equipped with a PLL.

The differences in the rotating angle and the unknown asymmetric transmission impedance result in cross-axis coupling interference during data demodulation. Specifically, signals modulated on the d-axis at the transmitter are coupled to both the d and q axes at the receiver, and the same occurs for q-axis data. The major challenges involve handling strongly coupled cross-axis interference, accurately extracting the coupling network parameters for decoupling, and achieving real-time decoupling that adapts to varying system conditions. To overcome these challenges, this article proposes a decoupling strategy that employs pilot carrier signals to establish a coupling matrix H for each communication round. By multiplying the demodulated signal $\tilde{V}_{\mathrm{R}}^{dq'}$ with H^{-1}, the axis-coupling effect can be eliminated. Here, $\tilde{V}_{\mathrm{R}}^{dq'}$ refers to the voltage phasor of the carrier signal in the d–q frame, i.e.,

$$\tilde{V}_{\mathrm{R}}^{d'} = A_d\, e^{j\phi_d},\ \tilde{V}_{\mathrm{R}}^{q'} = A_q\, e^{j\phi_q} \tag{1}$$

where A_d and A_q are the root-mean-square (RMS) amplitudes of the received carrier signal, and ϕ_d and ϕ_q are their phases. Through the proposed decoupling strategy, the original data

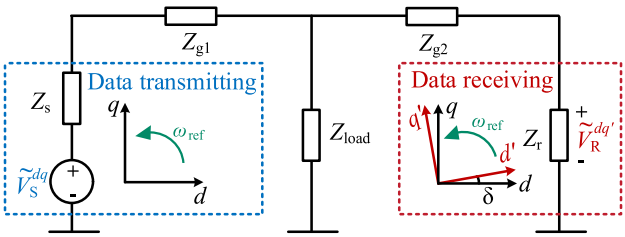

Fig. 5. Single-line diagram of the communication model of a three-phase system in *d–q* frame.

added on the *d* and *q* axes can be accurately restored by identifying the phase of $\tilde{V}_{\mathrm{S}}^{dq'}$. The decoupling strategy will be introduced in detail in Section III-B.

III. Principle of the Decoupling Strategy

The communication model is analyzed in this section to discuss the two main reasons for the cross-axis coupling interference in detail. Furthermore, a dedicated decoupling and demodulation strategy is introduced to estimate and eliminate the cross-axis coupling issue.

A. Communication Model

For the sake of simplification, a communication model featuring a two-node system is developed in Fig. 5 to analyze the signal transmission process. The data transmitter is represented as a voltage source $\tilde{V}_{\mathrm{S}}^{dq}$ in series with an internal impedance Z_{s} through a Thévenin equivalent. It is worth noting that the voltage source refers to the signal generator rather than the actual high-voltage ac generation. Here, $\tilde{V}_{\mathrm{S}}^{dq}$ is the phasor representation of the signal, i.e.,

$$\tilde{V}_{\mathrm{S}}^{dq} = \begin{bmatrix} A e^{\mathrm{j}\phi_d} \\ A e^{\mathrm{j}\phi_q} \end{bmatrix} \text{ and } V_{\mathrm{S}}^{dq}(t) = \begin{bmatrix} \sqrt{2}A\cos(\omega_c t + \phi_d) \\ \sqrt{2}A\cos(\omega_c t + \phi_q) \end{bmatrix} \quad (2)$$

where A is the RMS amplitude of the signal, ϕ_d and ϕ_q are the phases from QPSK, and ω_c is the angular frequency of the carrier signal. Z_{g1} and Z_{g2} denote the line impedances, Z_{load} represents the power load, and Z_r represents the impedance of the data-receiving inverter. Two facts need to be noted: the transmission model is established at the communication carrier frequency ω_c. As a result, all impedance elements are numerical values at $s = j\omega_c$ and the model is established in the *d–q* frame, i.e., all impedance elements are 2×2 matrices in the *d–q* frame. For example, for a line consisting of resistance *R* and inductance *L*, its impedance Z_{line} is

$$Z_{\mathrm{line}} = \begin{bmatrix} R + j\omega_c L & -\omega_0 L \\ \omega_0 L & R + j\omega_c L \end{bmatrix} \quad (3)$$

where ω_0 is the grid frequency.

In general, if the receiving inverter can correctly acquire information of ϕ_d and ϕ_q, the data can be restored. However, two major obstacles limit accurate data reception. First, the impedance of the data transmitting inverter, the data receiving inverter, as well as the lines and loads, significantly affect the signal at the receiving end. Through circuit analysis, it is straightforward to have the voltage on Z_r

$$\tilde{V}_R^{dq} = T_Z \cdot \tilde{V}_S^{dq} \quad (4)$$

where T_Z is

$$T_Z = \frac{(Z_{g2} + Z_r) // Z_{\mathrm{load}}}{Z_s + Z_{g1} + (Z_{g2} + Z_r) // Z_{\mathrm{load}}} \cdot \frac{Z_r}{Z_{g2} + Z_r} \quad (5)$$

and can be expressed as

$$T_{\mathrm{Z}} = \begin{bmatrix} T_{\mathrm{Z}dd} & T_{\mathrm{Z}dq} \\ T_{\mathrm{Z}qd} & T_{\mathrm{Z}qq} \end{bmatrix}. \quad (6)$$

In practice, T_Z is unknown. For the lines and loads, although the information is possessed by the system operator, such information is typically not shared with inverters. Furthermore, due to the presence of the droop controller, or PLL controller for the grid-following inverter, Z_s and Z_r are typically asymmetric, making T_Z an asymmetric matrix.

Second, $\tilde{V}_R^{dq}$ is not the final result seen by the data receiver. Each inverter transfers the terminal voltage from the *abc* frame to the *dq* frame from a rotating angle θ generated by its own droop or PLL controller, which uses the voltage measured locally. Consequently, such a rotating reference frame is aligned to the local voltage angle. At different locations of the system, the bus voltage angle will be different, depending on the power flow (generations, lines, loads, etc.). Hence, at the receiving end, the local frame dq' is expected to be aligned to a different angle, leading to an angle difference δ between dq' and dq. With the effect of δ, the actual signal seen by the data receiver is

$$\tilde{V}_R^{dq'} = T_\delta \, \tilde{V}_R^{dq} \quad (7)$$

where T_δ is the rotating matrix expressed as

$$T_\delta = \begin{bmatrix} \cos\delta & \sin\delta \\ -\sin\delta & \cos\delta \end{bmatrix}. \quad (8)$$

Again, although known by the system operator, the information of δ is not necessarily to be shared with inverters.

Combining (4) and (7), the final signal received by the data receiver is

$$\tilde{V}_R^{dq'} = T_\delta \, T_Z \tilde{V}_S^{dq}. \quad (9)$$

The term $T_Z T_\delta$ will lead to the cross-axis coupling effect on the received signal, and we define the coupling matrix as

$$H = T_\delta \, T_Z = \begin{bmatrix} H_{dd} & H_{dq} \\ H_{qd} & H_{qq} \end{bmatrix}. \quad (10)$$

With H unknown, the data receiver is not able to acquire the original information of ϕ_d and ϕ_q and hence cannot restore the data. Moreover, H varies according to the change of system operating point, making it even more complicated to establish a reliable communication link. To address this challenge, a decoupling strategy is proposed to estimate the coupling matrix H and enable accurate data demodulation.

B. Decoupling and Demodulation Strategy

The frame protocol of the data transmitting signals in the proposed decoupling strategy is described in Fig. 6, where two sets of carrier waveforms with the phase of 0 are added

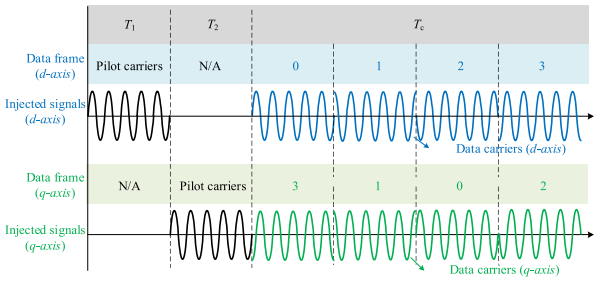

Fig. 6. Frame protocol of the data transmitting signals in the proposed decoupling strategy.

respectively on the *d*-axis and *q*-axis before transmitting the real data, namely the pilot carriers. For the period T_1, the pilot carrier is added on the *d*-axis while the *q*-axis remains silent, while the same pilot carrier is added on the *q*-axis for the period T_2, i.e.,

$$\tilde{V}_{\mathrm{S}(1)}^{dq} = \begin{bmatrix} Ae^{j0} \\ 0 \end{bmatrix} \quad \tilde{V}_{\mathrm{S}(2)}^{dq} = \begin{bmatrix} 0 \\ Ae^{j0} \end{bmatrix} \tag{11}$$

where the subscript (1) and (2) refers to the signal in T_1 and T_2, respectively. The signals received by the data receiver during the two periods are

$$\tilde{V}_{R(1)}^{dq'} = \begin{bmatrix} \tilde{V}_{R,d(1)}^{dq'} \\ \tilde{V}_{R,q(1)}^{dq'} \end{bmatrix} \quad \tilde{V}_{R(2)}^{dq'} = \begin{bmatrix} \tilde{V}_{R,d(2)}^{dq'} \\ \tilde{V}_{R,q(2)}^{dq'} \end{bmatrix}. \tag{12}$$

Combining (9)–(12) yields

$$\begin{bmatrix} \tilde{V}_{R,d(1)}^{dq'} & \tilde{V}_{R,d(2)}^{dq'} \\ \tilde{V}_{R,q(1)}^{dq'} & \tilde{V}_{R,q(2)}^{dq'} \end{bmatrix} = \begin{bmatrix} H_{dd} & H_{dq} \\ H_{qd} & H_{qq} \end{bmatrix} \begin{bmatrix} Ae^{j0} & 0 \\ 0 & Ae^{j0} \end{bmatrix} \tag{13}$$

and

$$H = \frac{1}{A} \begin{bmatrix} \tilde{V}_{R,d(1)}^{dq'} & \tilde{V}_{R,d(2)}^{dq'} \\ \tilde{V}_{R,q(1)}^{dq'} & \tilde{V}_{R,q(2)}^{dq'} \end{bmatrix} \tag{14}$$

from which the coupling matrix H can be estimated before receiving the real data. In such a way, the signal can be decoupled via

$$\tilde{V}_S^{dq'} = H^{-1}\, \tilde{V}_R^{dq'} \tag{15}$$

and therefore, the data can be restored. Although the amplitude A may be unknown to the data receiver, it would not affect the phase information for data restoration and can be assumed to be 1 for simplicity. In practice, pilot carriers are placed at the beginning of each data frame to enable continuous re-estimation of H, thereby accommodating slow variations in system operating conditions. Rapid transients, however, may cause a mismatch between the estimated and actual H, potentially leading to demodulation errors. Reducing the frame length or inserting mid-frame pilot carriers can improve tracking performance under rapid transients. However, increasing the frequency of pilot intervals also introduces greater overhead, which requires a tradeoff.

The full process of the proposed decoupling strategy, as well as the signal demodulation process, is demonstrated in Fig. 7. The time-domain signal $v_d(t)$ and $v_q(t)$ are the power filter capacitor voltage of the data receiver in the *d–q* frame. They are multiplied by the locally generated complex sinusoidal signal, respectively. The results are filtered by the LPF and then reconstructed as complex numbers, transforming time-domain signals into phasors. Subsequently, all phasors are amplified by the integrator for computational convenience. During the pilot carrier periods T_1 and T_2, all elements of the coupling matrix H are estimated and stored in the memory. Subsequently, switches S_1 and S_2 are toggled. The data phasors are then multiplied by the inverse of the coupling matrix H^{-1} to achieve decoupling between *d* and *q* frames. The results contain the original phases of carrier signals at the data transmitter, which can be directly calculated. Finally, data decision modules are employed to restore the data.

IV. Experimental Verifications

A. Simulation Results

The proposed decoupling strategy is based on the communication model in Section III. Hence, a simulation prototype is built to verify the correctness of the theoretical model analysis. The schematic of the communication model is shown in Fig. 5, where Z_s= 0.1 Ω + 1 mH, Z_{g1}= 0.1 Ω + 1.2 mH, Z_{load}= 1 Ω + 1 mH, Z_{g2}= 0.47 Ω + 2 mH, Z_r = 0.15 Ω +1 mH, and the sending signals $\tilde{V}_{\mathrm{S}}^{dq}$ is set to (i) $\frac{1}{\sqrt{2}}\begin{bmatrix} e^{j(\frac{\mathrm{pi}}{3})} \\ e^{j(\frac{\mathrm{pi}}{6})} \end{bmatrix}$, (ii) $\frac{1}{\sqrt{2}}\begin{bmatrix} e^{j(\frac{5\mathrm{pi}}{6})} \\ e^{j(\frac{2\mathrm{pi}}{3})} \end{bmatrix}$, (iii) $\frac{1}{\sqrt{2}}\begin{bmatrix} e^{j(\frac{4\mathrm{pi}}{3})} \\ e^{j(\frac{7\mathrm{pi}}{6})} \end{bmatrix}$, and (iv) $\frac{1}{\sqrt{2}}\begin{bmatrix} e^{j(\frac{11\mathrm{pi}}{6})} \\ e^{j(\frac{5\mathrm{pi}}{3})} \end{bmatrix}$. The angle difference δ of the *d–q* frames between the data transmitting and data receiving ends is set to δ= 30°. The coupling matrix can be calculated given the system impedance and the angle difference from (10), and its value is

$$H = \begin{bmatrix} 0.074 - j0.0055 & 0.042 - j0.0033 \\ -0.042 + j0.0033 & 0.074 - j0.0055 \end{bmatrix}.$$

Fig. 8 presents the theoretical receiver signals based on the impedance coupling matrix T_Z, the theoretical signals incorporating the full coupling matrix H, and the expected receiver signals from the circuit model. These are distinguished by triangles, dots, and squares, respectively. Four groups of signals corresponding to the transmitted signals $\tilde{V}_S^{dq}$ are colored blue, green, red, and magenta. The results show that the theoretical signals based on the coupling matrix H closely match the expected receiver signals in amplitude and phase, whereas those based solely on T_Z do not. The simulation results verify the correctness of the analysis of the communication model. Due to the coupling matrix being usually unknown in practical ac systems, a decoupling strategy is proposed and experimentally verified in the experimental section.

B. Experimental Results

To validate the feasibility of the proposed TPC scheme, a 3.3 kW ac microgrid with three grid-forming inverters operating with 8 kHz switching frequency has been built, as shown in Figs. 9 and 10. Simulink software is employed to develop the

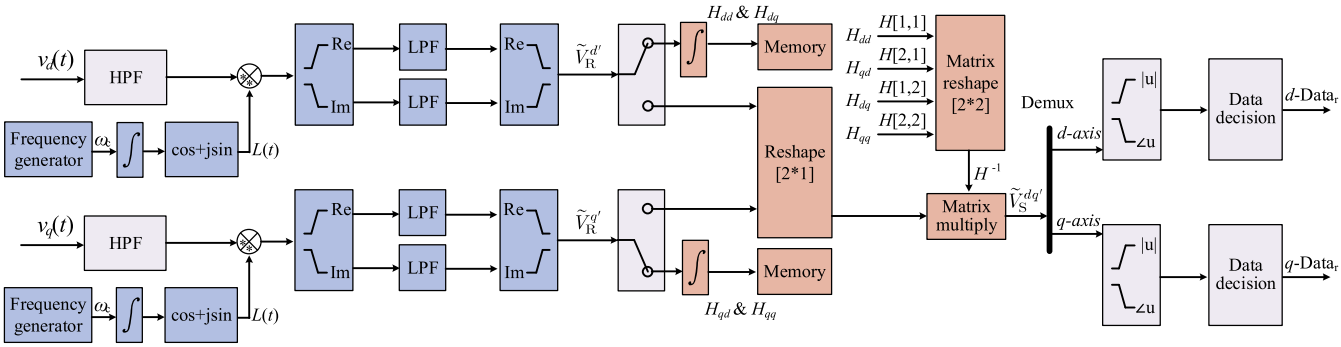

Fig. 7. Overall process of demodulation and decoupling.

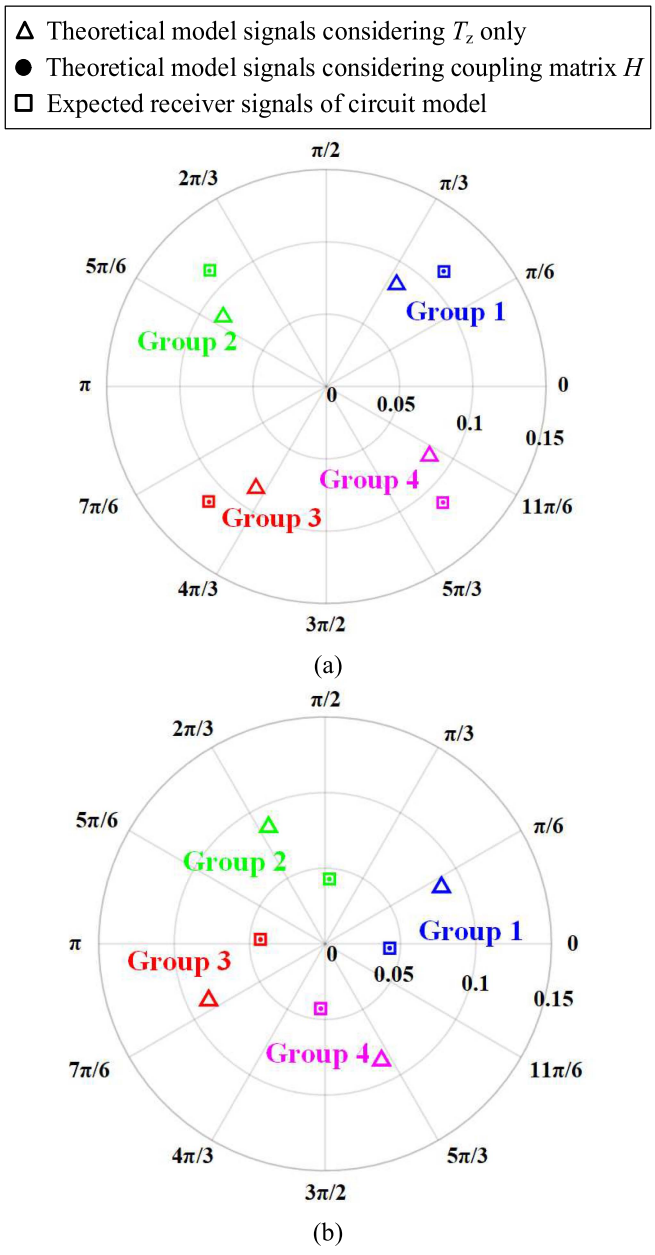

Fig. 8. Simulation results of receiving signals in polar coordinates at (a) d-axis and (b) q-axis.

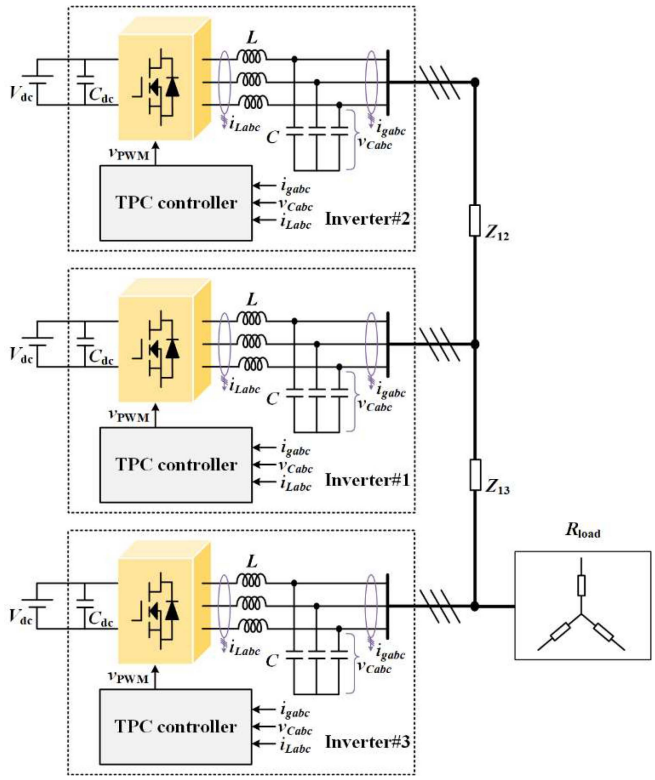

Fig. 9. Three-node three-phase inverter based TPC prototype diagram.

controllers of the three inverters. The main parameters are listed in Table I.

Droop control, along with voltage/current PI dual-loop control, is implemented for power conversion. The waveforms of operational frequency, power filter capacitor voltage, and active power are presented in Fig. 11. The experimental data are sampled at a frequency of 8 kHz and recorded using Simulink software. This sampling rule is applied to all subsequent experimental results. All three inverters have the same droop parameters; the stable frequency is around 49.945 Hz, while the peak-to-peak value of the power filter capacitor voltage measures about $220\sqrt{2} = 311$ V. The total active power is calculated as $P = 3 * 220^2/44 \approx 3.3$ kW, which is evenly distributed among three inverters. The data modulation and

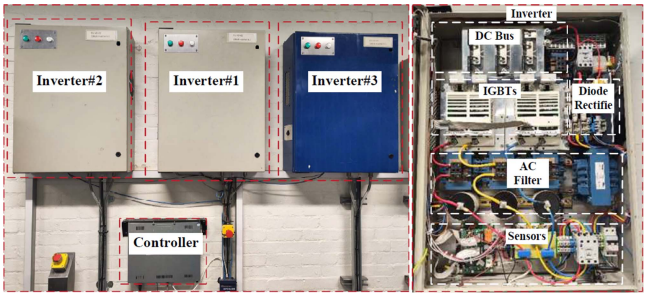

Fig. 10. Experimental test platform.

TABLE I
EXPERIMENT PARAMETERS

Parameter	Value
Rated DC voltage V_{dc}	650 V
Rated phase voltage V_{dc}	220 V
Rated LC filter capacitor C	50 μF
Rated LC filter inductance L	1.35 mH
Line impedance Z_{12}	0.1 Ω+ 1.2 mH
Line impedance Z_{13}	0.47 Ω + 1.2 mH
Grid frequency	50 Hz
Rated load resistance	44 Ω
Data carrier frequency f_c	1 kHz
Switching frequency	8 kHz

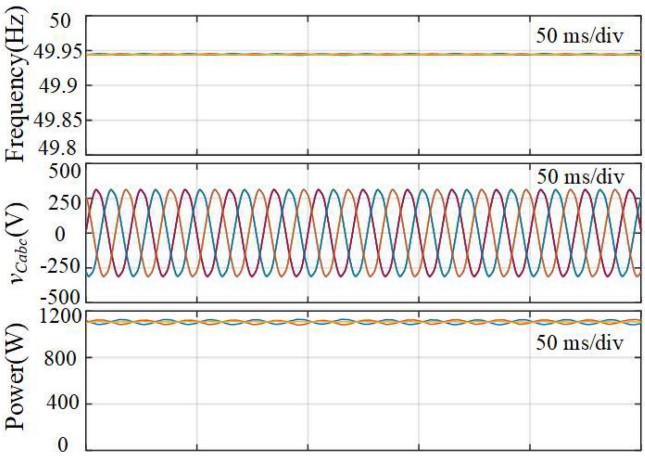

Fig. 11. Stable operation waveforms of three inverters.

demodulation functions are modularized, facilitating data transmission and reception by each inverter. In the experiments, the data is transmitted from inverter#1 and received by inverter#2. Taking bus-1 as the reference bus, the voltage angle δ at other buses can be calculated from power flow calculations using the Newton–Raphson method. For bus-2, $\delta \approx 7^\circ$, and

$$T_\delta = \begin{bmatrix} \cos 7^\circ & \sin 7^\circ \\ -\sin 7^\circ & \cos 7^\circ \end{bmatrix} = \begin{bmatrix} 0.9925 & 0.1219 \\ -0.1219 & 0.9925 \end{bmatrix}.$$

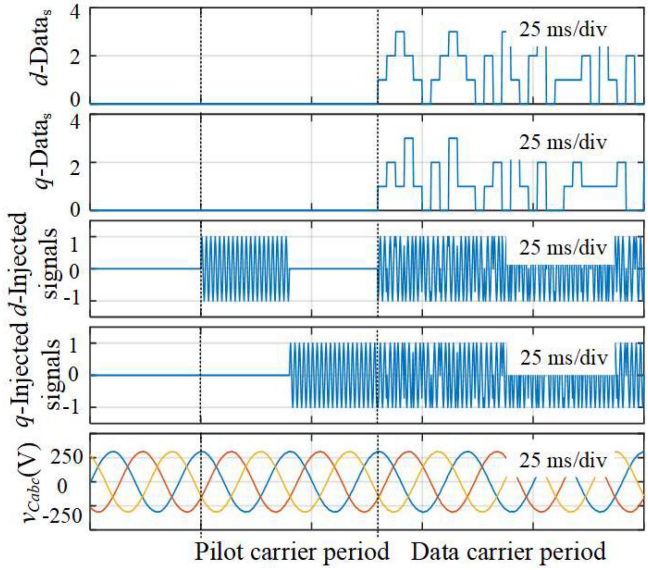

Fig. 12. Waveforms of inverter#1 when transmitting data.

Based on the structure shown in Fig. 9 and the example given in Section III-A, T_Z can be derived from circuit analysis as

$$T_Z = \frac{(Z_{12}//Z_{\text{inv2}})\,//\,(Z_{13}+Z_{\text{inv3}}//Z_{\text{load}})}{Z_{\text{inv1}}+(Z_{12}//Z_{\text{inv2}})\,//\,(Z_{13}+Z_{\text{inv3}}//Z_{\text{load}})} \cdot \frac{Z_{\text{inv2}}}{Z_{\text{inv2}}+Z_{12}}$$

where Z_{inv1}, Z_{inv2}, and Z_{inv3} are the impedance models of the three inverters around the given operating point. Substituting T_δ and T_Z into (10) yields the analytical expression of H. It is clear from the above equation that T_Z is dependent on the line impedance Z_{12}, Z_{13}, the load impedance Z_{load}, and the impedance model of the inverters: Although Z_{12}, Z_{13} and Z_{load}, which are formed by passive components (resistance and inductance), can be readily achieved from the parameters in Table I, Z_{inv1}, Z_{inv2}, and Z_{inv3} are typically unknown in practice. As a result, the theoretical value of H is generally unachievable in practice. Alternatively, the proposed method, which derives the coupling matrix H in real time using only measurements, offers a practical and effective solution.

Fig. 12 illustrates the waveforms of inverter#1 during data transmission. The waveforms, arranged from top to bottom, represent the data in the d axis, the data in the q-axis, the normalized injected signals in the d-axis, the normalized injected signals in the q axis, and the power filter capacitor voltages v_{Cabc}, respectively. Data in both d and q axes is modulated as normalized injected signals, including pilot carriers and data carriers that follow the frame protocol depicted in Fig. 6. The injected signals are amplitude-controllable and superimposed onto the power reference before dq/abc transformation. Small perturbations can be observed in both the waveforms of v_{Cabc} from the onset of the pilot carrier. The frequency of carrier signals is set at 1 kHz with a symbol duration of 2 ms, resulting in a calculated bitrate of BR $= 2 \times 500 \times \log_2 4 = 2$ kbps. The data transmission rate can be further improved by increasing

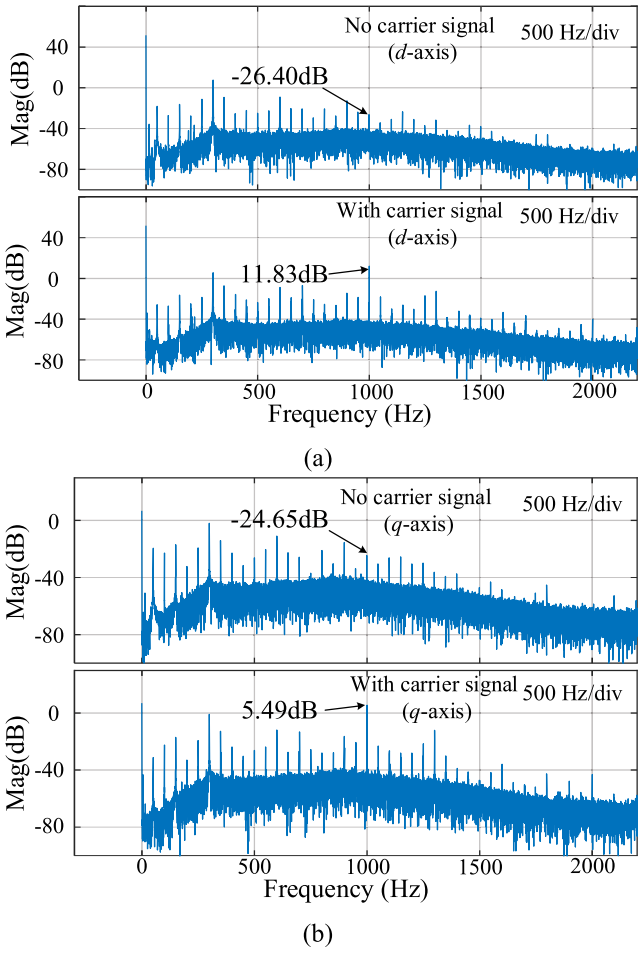

Fig. 13. Frequency spectrum of the capacitor voltage in the d–q axes of inverter#2. (a) d-axis waveforms. (b) q-axis waveforms.

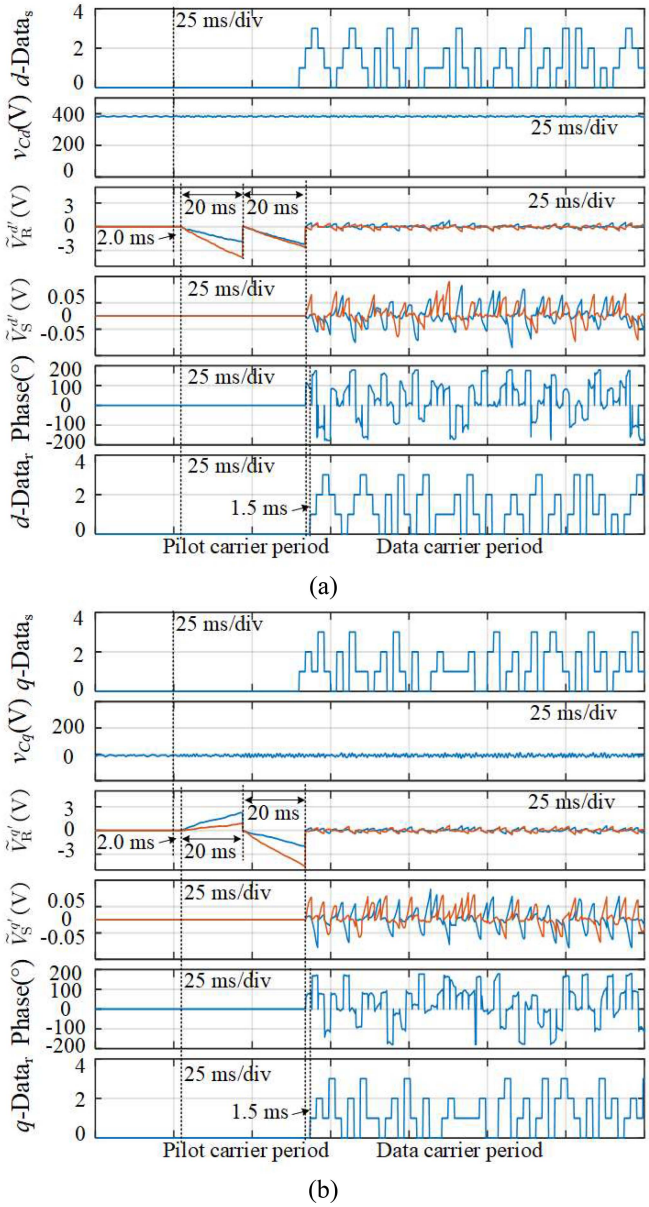

Fig. 14. Waveforms of inverter#2 when receiving data. (a) d-axis waveforms. (b) q-axis waveforms.

the switching frequency, as it is linearly proportional to the switching frequency. A higher data transmission rate would increase the scalability of communication among inverters.

Fig. 13 illustrates the frequency spectrum of the capacitor voltage in the d and q axes when the carrier signals are present and not present, respectively. When the carrier signal is not present, the line-line voltage rms value corresponding to 380 V is reflected as 51.67 dB. When the carrier signal is present, the amplitude at approximately 1 kHz measures about 11.83 dB in the d-axis and 5.49 dB in the q-axis, which corresponds to about 1% and 0.5% of the fundamental component of the line-line voltage.

Fig. 14 illustrates the transmitted data from inverter#1, the capacitor voltage in the d and q axes of inverter#2, the real and imaginary parts of the phasors $\tilde{V}_R^{dq'}$, the real and imaginary parts of the decoupled phasors $\tilde{V}_S^{dq'}$, the restored phase of inverter#2, and the result of data decision for inverter#2, respectively. During the pilot carrier period, the coupling matrix can be obtained by a twice 20-ms estimation process as shown in the figures of $\tilde{V}_R^{d'}$ and $\tilde{V}_R^{q'}$, where the real and imaginary parts are marked blue and orange, respectively. For the first estimation process, the pilot carrier is present solely in the d-axis of inverter#1, yielding the coupling matrix parameters of the d-axis of inverter#2 to the d axis of inverter#1 $H_{dd} = -1.846\text{-j}3.868$ and the q-axis of inverter#2 to the d axis of inverter#1 $H_{qd} = 2.249\text{+j}0.851$. Similarly, for the first estimation process, the pilot carrier is present solely in the q-axis of inverter#1, yielding $H_{dq} = \text{-}2.127\text{-j}2.614$ and $H_{qq} = -1.911\text{-j}4.561$. The value of the coupling matrix H is

$$H = \begin{bmatrix} -1.846 - \text{j}3.868 & -2.127 - \text{j}2.614 \\ 2.249 + \text{j}0.851 & -1.911 - \text{j}4.561 \end{bmatrix}.$$

An approximate delay of 2 ms can be observed in the waveforms of phasors $\tilde{V}_{\text{R}}^{d'}$ and $\tilde{V}_{\text{R}}^{q'}$, attributed to the digital filter. During the data carrier period, $\tilde{V}_{\text{R}}^{dq'}$ is multiplied by the inverse of the coupling matrix H^{-1} to realize decoupling. The decoupled

TABLE II
RESULTS OF ERROR RATE TESTING COMPARISON

Injection amplitude (p.u.)	0.01	0.015	0.02
SNR (dB, d-axis)	9.906	13.451	15.551
SNR (dB, q-axis)	12.503	16.216	18.631
BER with decoupling (d-axis)	2×10^{-4}	1×10^{-5}	$<1\times10^{-6}$
BER without decoupling (d-axis)	1.19×10^{-1}	1.06×10^{-1}	0.97×10^{-2}
BER with decoupling (q-axis)	2×10^{-4}	1×10^{-5}	$<1\times10^{-6}$
BER without decoupling (q-axis)	2.13×10^{-2}	1.84×10^{-2}	1.29×10^{-2}

results are complex phasors $\tilde{V}_S^{d'}$ and $\tilde{V}_S^{q'}$, where the real and imaginary parts are marked blue and orange, respectively. The restored phase value can be calculated from the complex phasors $\tilde{V}_S^{d'}$ and $\tilde{V}_S^{q'}$ by applying the arctan function. Data decisions are made at the position of 3/4 symbol cycles, resulting in an approximate delay of 1.5 ms; hence, the practical delay from transmitted data to received data is approximately 3.5 ms. The comparison of the received data with the transmitted data indicates that the results are correct, thereby validating the feasibility of the proposed scheme.

The signal-to-noise ratio (SNR) can be derived using (16), which is expressed as

$$\text{SNR} = 10\lg\left(\frac{P_s}{P_n}\right) \tag{16}$$

where P_s is the receiving signal power and P_n is the power of the additive white Gaussian noise. To evaluate the performance gain introduced by this decoupling process, we compared bit error rates (BER) under two conditions:

1) Without decoupling (setting the decoupling matrix as the unit matrix), where direct demodulation is performed.

2) With decoupling, where the proposed adaptive estimation and compensation are applied.

Under identical experimental settings (1 kHz carrier, 8 kHz switching frequency, 3.3 kW converter, 0.01, 0.015, and 0.02 injection amplitude), the results of SNR and the BER are listed in Table II and shown in Fig. 15. It can be observed that without the decoupling process, the BER (black and pink curves) exceeds 10^{-1}, indicating unreliable communication. In contrast, with the adaptive decoupling mechanism enabled (blue and red curves), the BER is significantly reduced, demonstrating the effectiveness of the proposed interference elimination strategy. The results also prove that with the proposed decoupling mechanism, the communication is robust under different SNR conditions.

To ensure reliable performance in power grids with high harmonic distortion, the proposed TPC method incorporates several robustness measures. First, the carrier frequency is flexibly configurable within the usable bandwidth (up to half the switching frequency), allowing it to avoid interference from harmonics. Second, a digital HPF is applied at the receiver to suppress low-frequency harmonic noise while preserving the

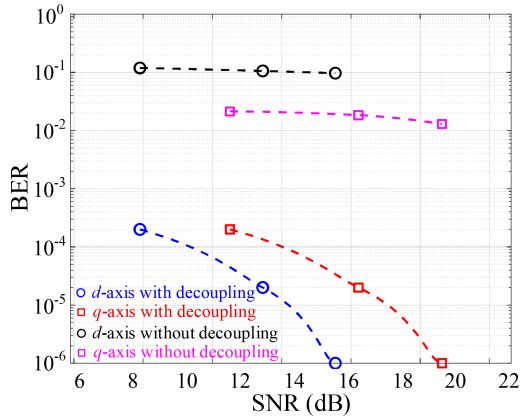

Fig. 15. Results of error rate testing before and after decoupling.

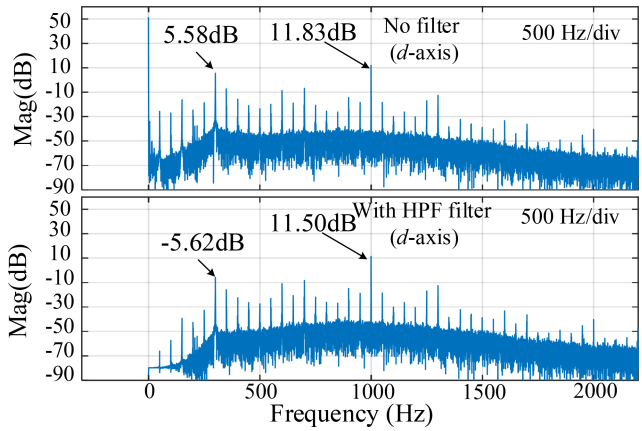

Fig. 16. Frequency spectrum of the d-axis capacitor voltage before and after the HPF filter.

TABLE III
LITERATURE COMPARISON

Reference	Modulation	Experimentally verified bitrate (bps)	Switching frequency utilization η	Injection amplitude (p.u.)
Shan and Umanand [24]	OOK	5	N/A	0.02-0.07
Liu et al. [25]	FSK	100	0.0067	0.0065
This work	QPSK	2000	0.25	0.01

communication carrier. For example, under a 1 kHz carrier, the 300 Hz harmonic component is attenuated by 11.2 dB after filtering, as shown in Fig. 16. The effect of the filter in the q-axis is the same and not shown for the sake of brevity. Finally, the TPC framework is compatible with advanced interference mitigation strategies such as adaptive carrier shifting or frequency-hopping, which can be implemented to further enhance resilience and merit further research. These features collectively ensure that the TPC scheme remains feasible and reliable in harmonic-rich power systems.

A comparison between the proposed TPC-CR method and existing TPC-CR methods is given in Table III. According to Table III, the proposed TPC-CR method achieves a decent

communication rate under a small data carrier injection amplitude through dual-channel decoupled QPSK modulation. The injection amplitude can be increased within allowable ripple constraints to improve signal strength when necessary. Meanwhile, high switching frequency utilization η (bitrate divided by switching frequency) rate indicates that the communication rate can be further increased with the increase of the switching frequency utilization.

V. Conclusion

This article presents a dual-channel decoupled data modulation method to realize TPC in three-phase ac systems, where power buses are multiplexed as communication channels, eliminating the need for additional communication cables or hardware. This approach simplifies system structure and enhances reliability. A thorough analysis of cross-axis coupling interference is provided, along with an adaptive estimation strategy that effectively mitigates this issue. By decoupling two communication channels and enabling simultaneous data modulation through a single inverter, the method improves both channel utilization and communication rate. Experimental results from multiple inverters verified the theoretical analysis and demonstrated a 2-kbps bitrate on a 3.3 kW system, validating the proposed method's effectiveness. While the proposed method demonstrates reliable performance, further enhancements such as error correction and retransmission schemes may be explored to improve robustness in complex grid environments.

References

[1] M. Liserre, T. Sauter, and J. Y. Hung, "Future energy Systems: Integrating renewable energy sources into the smart power grid through industrial electronics," *IEEE Ind. Electron. Mag.*, vol. 4, no. 1, pp. 18–37, Mar. 2010, doi: 10.1109/MIE.2010.935861.

[2] D. Vinnikov, A. Chub, E. Liivik, R. Kosenko, and O. Korkh, "Solar Optiverter—A novel hybrid approach to the photovoltaic module level power electronics," *IEEE Trans. Ind. Electron.*, vol. 66, no. 5, pp. 3869–3880, May 2019, doi: 10.1109/TIE.2018.2850036.

[3] Y. Li and J. Yan, "Cybersecurity of smart inverters in the Smart grid: A survey," *IEEE Trans. Power Electron.*, vol. 38, no. 2, pp. 2364–2383, Feb. 2023, doi: 10.1109/TPEL.2022.3206239.

[4] Y. Gu and T. C. Green, "Power system stability with a high penetration of inverter-based resources," *Proc. IEEE*, vol. 111, no. 7, pp. 832–853, Jul. 2023, doi: 10.1109/JPROC.2022.3179826.

[5] S. Galli, A. Scaglione, and Z. Wang, "For the grid and through the grid: The role of power line communications in the smart grid," *Proc. IEEE*, vol. 99, no. 6, pp. 998–1027, Jun. 2011, doi: 10.1109/JPROC.2011.2109670.

[6] X. He, R. Wang, J. Wu, and W. Li, "Nature of power electronics and integration of power conversion with communication for talkative power," *Nat. Commun.*, vol. 11, no. 1, pp. 2479, May 2020, doi: 10.1038/s41467-020-16262-0.

[7] R. Wang, X. He, J. Wu, R. Zhang, and W. Li, "Power and signal dual modulation with info nature of Power converters," *IEEE J. Emerg. Sel. Topics Power Electron.*, vol. 11, no. 1, pp. 588–601, Feb. 2023, doi: 10.1109/JESTPE.2022.3199099.

[8] M. Liserre, H. Beiranvand, Y. Leng, R. Zhu, and P. A. Hoeher, "Overview of talkative power conversion technologies," *IEEE Open J. Power Electron.*, vol. 4, pp. 67–80, 2023, doi: 10.1109/OJPEL.2023.3237709.

[9] R. Han and D. J. Rogers, "Zero-additional-hardware power line communication for DC–DC converters," *IEEE Trans. Power Electron.*, vol. 37, no. 11, pp. 13107–13118, Nov. 2022, doi: 10.1109/TPEL.2022.3178020.

[10] Y. Zhu, J. Wu, R. Wang, Z. Lin, and X. He, "Embedding power line communication in photovoltaic optimizer by modulating data in power control loop," *IEEE Trans. Ind. Electron.*, vol. 66, no. 5, pp. 3948–3958, May 2019, doi: 10.1109/TIE.2018.2838081.

[11] Y. Guan, J. Wu, K. Liu, K. Zhao, and X. He, "Multi-input PV optimizer system with built-in communication using talkative power conversion," *IEEE J. Emerg. Sel. Topics Power Electron.*, vol. 12, no. 4, pp. 3392–3401, Aug. 2024, doi: 10.1109/JESTPE.2024.3363208.

[12] H.-P. Park, H. Choi, M. Kim, and S. Chae, "Multi-sinusoidal perturbation strategy for BPSK power line communication and online battery impedance measurement," *IEEE J. Emerg. Sel. Topics Power Electron.*, vol. 12, no. 4, pp. 3360–3371, Aug. 2024, doi: 10.1109/JESTPE.2023.3343589.

[13] F. Wang, D. Yuan, and X. Zhang, "Low-voltage inbound powerline communication based on talkative power conversion," *IEEE J. Emerg. Sel. Topics Power Electron.*, vol. 12, no. 4, pp. 3348–3359, Aug. 2024, doi: 10.1109/JESTPE.2024.3357858.

[14] H.-J. Choi and J.-H. Jung, "Enhanced power line communication strategy for DC microgrids using switching frequency modulation of power converters," *IEEE Trans. Power Electron.*, vol. 32, no. 6, pp. 4140–4144, Jun. 2017, doi: 10.1109/tpel.2017.2648848.

[15] R. Zhang, Y. Hui, J. Wu, R. Wang, Z. Lin, and X. He, "Embedding OFDM-based carrier communication into power control loop of converter in DC microgrids," *IEEE Trans. Ind. Electron.*, vol. 69, no. 7, pp. 6914–6924, Jul. 2022, doi: 10.1109/TIE.2021.3095821.

[16] Y. Leng, D. Yu, K. Han, S. S. Yu, and Y. Hu, "OFDM-based intrinsically safe power and signal synchronous transmission for CC-PT-controlled buck converters," *IEEE Trans. Power Electron.*, vol. 37, no. 9, pp. 10319–10331, Sep. 2022, doi: 10.1109/TPEL.2022.3164240.

[17] J. Chen, K. Liu, J. Wu, R. Wang, W. Weng, and X. He, "Simultaneous power and data transmission using combined three degrees of freedom modulation strategy in DC–DC converters," *IEEE Trans. Power Electron.*, vol. 38, no. 3, pp. 3191–3200, Mar. 2023, doi: 10.1109/TPEL.2022.3226468.

[18] K. Liu, Y. Hui, J. Chen, J. Wu, and X. He, "Simultaneous power and data modulation scheme for LLC resonant converter," *IEEE Trans. Power Electron.*, vol. 39, no. 1, pp. 270–279, Jan. 2024, doi: 10.1109/TPEL.2023.3321120.

[19] K. Liu, H. Yang, Y. Chen, Y. Hui, J. Wu, and X. He, "Active Rectified LLC resonant converter using combined frequency and phase modulation for talkative power conversion," *IEEE J. Emerg. Sel. Topics Power Electron.*, vol. 12, no. 4, pp. 3315–3324, Aug. 2024, doi: 10.1109/JESTPE.2024.3380264.

[20] J. Chen, J. Wu, R. Wang, R. Zhang, and X. He, "Coded PWM based switching ripple communication applied in visible light communication," *IEEE Trans. Power Electron.*, vol. 36, no. 8, pp. 9659–9667, Aug. 2021, doi: 10.1109/TPEL.2021.3056754.

[21] Y. Leng, R. Zhu, M. Liserre, and P. A. Hoeher, "Variable zero-vector-width-based three-phase DC/AC talkative power conversion," *IEEE J. Emerg. Sel. Topics Power Electron.*, vol. 12, no. 4, pp. 3402–3414, Aug. 2024, doi: 10.1109/JESTPE.2024.3396924.

[22] Y. Zhang, G. Chen, Y. Hu, C. Gong, and Y. Wang, "Cascaded multilevel inverter based power and signal multiplex transmission for electric vehicles," *CES Trans. Elect. Machines Syst.*, vol. 4, no. 2, pp. 123–129, Jun. 2020, doi: 10.30941/CESTEMS.2020.00017.

[23] Z. Wang, D. Zhou, X. Liu, Z. Shen, and J. Zou, "Sideband harmonic-based talkative power conversion," *IEEE Trans. Power Electron.*, vol. 39, no. 10, pp. 13708–13719, Oct. 2024, doi: 10.1109/TPEL.2024.3415425.

[24] S. Shan and L. Umanand, "A novel fractional harmonic d\text–q domain based power line signaling technique for power converters in a microgrid," *IEEE Trans. Power Electron.*, vol. 34, no. 11, pp. 11264–11277, Nov. 2019, doi: 10.1109/TPEL.2019.2895747.

[25] H. Liu, Y. Leng, and D. Yu, "Power & signal synchronous transmission strategy for three-phase voltage source inverter," in *Proc. Int. Joint Conf. Energy, Elect. Power Eng.*, 2022, pp. 145–153, doi: 10.1007/978-981-19-1922-0_12.

Keming Liu (Graduate Student Member, IEEE) received the B.S. degree in electrical engineering from Zhejiang University, Hangzhou, China, in 2021. He is currently working toward the Ph.D. degree in electrical engineering with the College of Electrical Engineering, Zhejiang University, Hangzhou, China.

From 2023 to 2024, he was a Visiting Ph.D. Student with Imperial College London, London, U.K. His current research interests include distributed power electronics systems and communication techniques applied in power electronics.

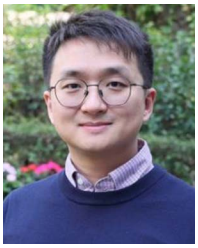

Yue Zhu (Member, IEEE) received the B.Eng. and M.Sc. degrees in electrical engineering from Zhejiang University, Hangzhou, China, in 2016 and 2019, respectively, and the Ph.D. degree in electrical engineering from Imperial College London, London, U.K., in 2022.

He was a Postdoctoral Research Associate with Imperial College London. He is currently an Assistant Professor with City University of Hong Kong, under the Presidential Assistant Professors Scheme. His research interests include dynamics and stability analysis of inverter-dominated power systems, data-driven impedance identification technology and analysis of system strength for inverter connection assessment.

Yunjie Gu (Senior Member, IEEE) received the B.Sc. and Ph.D. degrees in electrical engineering from Zhejiang University, Hangzhou, China, in 2010 and 2015, respectively.

He is currently an Assistant Professor with the Imperial College London and the Director of the M.Sc. Programme in Future Power Networks. Before his academic career, he was a Consulting Engineer with General Electric Global Research Centre, Shanghai, China. His research interests include stability theory for inverter-based power systems, stability-enhancing inverter technologies, and numerical methods for computer-aided stability analysis.

Jiande Wu (Senior Member, IEEE) was born in Zhejiang, China, in 1973. He received the B.Sc., M.Sc., and Ph.D. degrees in electrical engineering from the College of Electrical Engineering, Zhejiang University, Hangzhou, China, in 1994, 1997, and 2012, respectively.

Since 1997, he has been a Faculty Member with Zhejiang University, where he is currently an Associate Professor. From 2013 to 2014, he was an Academic Visitor with the University of Strathclyde, Glasgow, U.K. His research interests include power electronics control, distributed power electronics system and fieldbus communication.

Ruichi Wang (Senior Member, IEEE) received the B.Sc. and Ph.D. degree in electrical engineering from Zhejiang University, Hangzhou, China, in 2013 and 2019, respectively.

She is currently a Lecturer with Wolfson School of Mechanical, Electrical and Manufacturing Engineering, Loughborough, U.K. Her current research interests include power electronics and its control with communication integration for distributed systems.

Xiangning He (Fellow, IEEE) received the B.Sc. and M.Sc. degrees from Nanjing University of Aeronautical and Astronautical, Nanjing, China, in 1982 and 1985, respectively, and the Ph.D. degree in electrical engineering from Zhejiang University, Hangzhou, China, in 1989.

In 1991, he obtained a Fellowship from the Royal Society of U.K., and conducted research in Heriot-Watt University, Edinburgh, U.K., as a Post-Doctoral Research Fellow for two years. In 1994, he was an Associate Professor with Zhejiang University. Since 1996, he has been a Full Professor with the College of Electrical Engineering, Zhejiang University. His research interests are power electronics and their industrial applications.